**Title**
Site-Controlled Growth of Monolithic InGaAs/InP Quantum Well Nanopillar Lasers on Silicon



**Journal**
Nano Letters, 17(4)

**ISSN**
1530-6984 1530-6992

**Authors**
Schuster, Fabian
Kapraun, Jonas
Malheiros-Silveira, Gilliard N
et al.

**Publication Date**
2017-03-22

**DOI**
10.1021/acs.nanolett.7b00607

Peer reviewed

NANO LETTERS

Letter

pubs.acs.org/NanoLett

# Site-Controlled Growth of Monolithic InGaAs/InP Quantum Well Nanopillar Lasers on Silicon

Fabian Schuster, Jonas Kapraun, Gilliard N. Malheiros-Silveira, Saniya Deshpande, and Connie J. Chang-Hasnain*

Department of Electrical Engineering and Computer Sciences, University of California, Berkeley, California 94720, United States

Supporting Information

**ABSTRACT:** In this Letter, we report the site-controlled growth of InP nanolasers on a silicon substrate with patterned $SiO_2$ nanomasks by low-temperature metal−organic chemical vapor deposition, compatible with silicon complementary metal−oxide−semiconductor (CMOS) post-processing. A two-step growth procedure is presented to achieve smooth wurtzite faceting of vertical nanopillars. By incorporating InGaAs multiquantum wells, the nanopillar emission can be tuned over a wide spectral range. Enhanced quality factors of the intrinsic InP nanopillar cavities promote lasing at 0.87 and 1.21 μm, located within two important optical telecommunication bands. This is the first demonstration of a site-controlled III−V nanolaser monolithically integrated on silicon with a silicon-transparent emission wavelength, paving the way for energy-efficient on-chip optical links at typical telecommunication wavelengths.

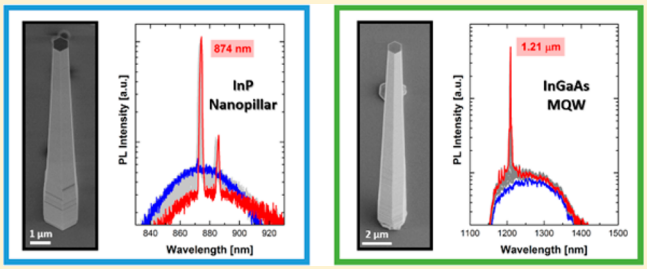


**KEYWORDS:** *Site-selective growth, nanopillars, laser, InP, quantum well, InGaAs*

Optical communication experienced a remarkable evolution during the past decade with a strong demand for infrared laser sources, especially in the spectral bands centered at 0.85, 1.3, and 1.55 μm where glass fibers feature low attenuation and low dispersion. High potential is seen in an integration of III−V materials on silicon, combining the advantages of a widely tunable, direct bandgap material featuring doping versatility with a silicon platform. However, the large lattice mismatch between III−V materials and silicon represents a natural barrier for heteroepitaxy which is difficult to overcome. Therefore, vertical III−V nanopillars are a matter of intense research, featuring a small footprint toward the substrate, a high crystal quality, potential for device miniaturization, and an intrinsic optical cavity.

The bottom-up growth of random III−V nanoneedles on silicon substrates has been developed by our group in recent years, culminating in the first room temperature InGaAs nanolaser monolithically integrated on silicon.[1] Further advances have been made in utilizing InP nanoneedles on silicon, e.g., optically pumped lasing,[2,3] and solar cells taking advantage of a significantly lower surface recombination compared to As-based materials.[4] This growth process does not involve foreign catalysts, and the applied temperatures are considered within the thermal budget of silicon-based complementary metal−oxide−semiconductor (CMOS) post-processing.[5,6] However, the statistical nature of nucleation is problematic, and it would be highly desirable to define the position of individual nanopillars and arrange them in regular arrays as building blocks for III−V optoelectronic devices on a silicon platform.

Homoepitaxial selective area growth (SAG), that is, homogeneous InP nanopillar arrays on masked InP substrates, is already a vibrant research field with pioneering work on Au-catalyzed growth,[7−11] self-catalyzed growth,[12−17] and nanopillar solar cells.[18−20] Despite the high crystal quality, optical lasing could only be achieved by releasing the nanopillars from their substrate in order to improve the reflection at the bottom interface.[21] In contrast, attempts of heteroepitaxial SAG, i.e., InP nanopillars on silicon substrates, are sparse. Watanabe et al. demonstrated selectivity with a Au-catalyzed process which lacked site-control of individual nanopillars as well as a homogeneous InP crystal orientation.[22] Wang et al. applied nanotrenches in a $SiO_2$ mask and deposited an additional Germanium seed layer to achieve the site-controlled growth of a InP nanopillar optical laser in a nonvertical direction.[23] In addition, neither attempt is compatible with state-of-the-art silicon CMOS technology. The challenge of integrating vertical InP nanopillar arrays with a silicon platform remains unsolved to the present day.

In this Letter, the site-controlled growth of vertical InP nanopillars on silicon will be demonstrated for the first time by utilizing $SiO_2$ nanomasks. A two-step growth process is presented to enhance the intrinsic nanopillar cavity by promoting regular wurtzite faceting and low tapering angles at CMOS-compatible growth temperatures. High-quality material is obtained as attested by the lasing characteristics of as-

**Received:** February 13, 2017
**Revised:** March 21, 2017
**Published:** March 22, 2017





DOI: 10.1021/acs.nanolett.7b00607
*Nano Lett.* 2017, 17, 2697−2702

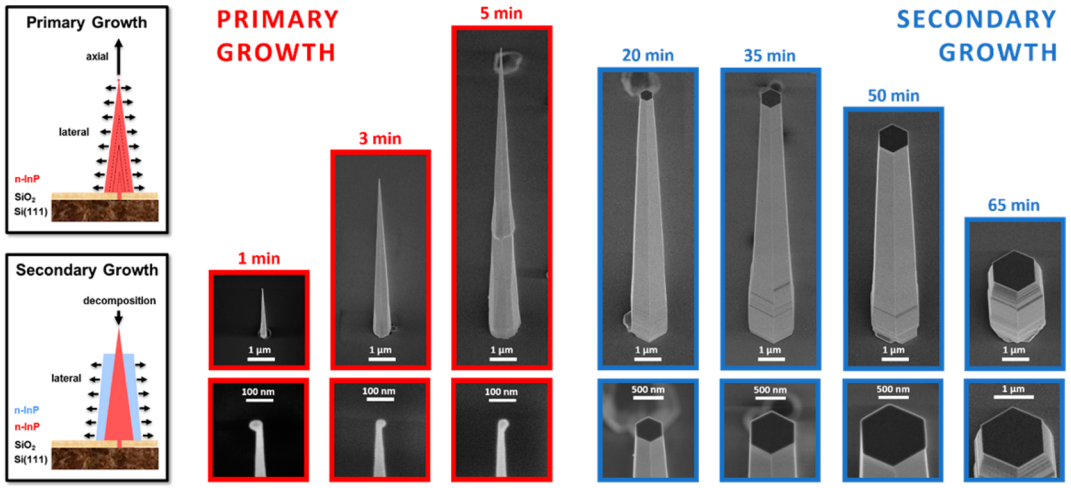


**Figure 1.** Evolution of n-InP SAG nanopillars on $SiO_2$/silicon nanomasks by using a two-step growth procedure: SEM images of (left) the primary growth after 1, 3, and 5 min growth time and of (right) of the secondary growth after 20, 35, 50, and 65 min growth time. The bottom row shows high magnification images of the respective nanopillar tops.

grown InP SAG nanopillars. In addition, we demonstrate control of the laser emission to silicon-transparent wavelengths by an incorporation of InGaAs quantum wells in the InP SAG nanopillars.

The nanomask fabrication was performed on 6″ n-type silicon (111) wafers, highlighting the scalability of the developed process. In a first step, 140 nm $SiO_2$ was deposited by plasma-enhanced chemical vapor deposition (PECVD). Subsequently, arrays of holes with different pitches, i.e., the distance from hole to hole, were defined by deep-UV lithography in a 5500/90 ASML stepper and transferred into the mask by reactive ion etching, resulting in hole diameters of 350 nm. Finally, the nanomask wafer was diced to 1 × 1 cm pieces for more convenient handling. Prior to growth, the substrates had to undergo a $SF_6$ plasma treatment (60 sccm, 10 s) to roughen the revealed silicon (111) surface in the holes followed by an $O_2$ plasma treatment (80 sccm, 10 s) to substitute the fluorine surface termination. Finally, the substrates were etched in buffered hydrofluoric acid for 5 s and loaded into vacuum.

The growth was performed by metal−organic chemical vapor deposition (MOCVD) in an EMCORE D75 showerhead reactor at a low pressure of 75 Torr utilizing standard source materials (TMI, TBP, TEGa, TBA, DETe). A schematic of the n-InP two-step growth process is given in Figure S1. Prior to growth the substrate is annealed in situ at 550 °C for 5 min under TBP atmosphere. Then, the primary growth is initiated at 460 °C by supplying TMI with a partial pressure of $6.4 \times 10^{-7}$ atm and TBP with a partial pressure of $7.0 \times 10^{-5}$ atm Subsequently, the secondary growth is performed at a higher temperature of 480 °C with TMI and TBP partial pressures of $1.2 \times 10^{-7}$ atm and $8.5 \times 10^{-5}$ atm, respectively. As dopants were found to negatively influence the nucleation, site-controlled growth was optimized with n-type nanopillars from the very beginning to pave the way for future work in optoelectronic devices. Thus, DETe is offered simultaneously during both growth steps with 2.5 sccm to ensure moderate n-type doping.

Scanning electron microscopy (SEM) was performed in an FEI Nova NanoSEM 650 system operated at 2 keV acceleration voltage and at a tilting angle of 30°. In Figure 1 the evolution of the n-InP primary growth in an array with 10 $\mu$m pitch is presented after 1, 3, and 5 min. It can be seen that nucleation takes place at the edge of the $SiO_2$ mask holes and expands rapidly in axial direction. Characteristic for these growth conditions is the tapered needle shape with pointy tip and irregular side faceting. In the high-resolution SEM images a droplet of approximately 30 nm is clearly resolved on all needle tips, indicating that nucleation is catalyzed by a liquid indium droplet. Consistently, a high asymmetry in growth rates is observed with 3.7 ± 0.3 $\mu$m/min in axial and 235 ± 15 nm/nm in lateral direction (Figure 2 left). The result is a core−shell

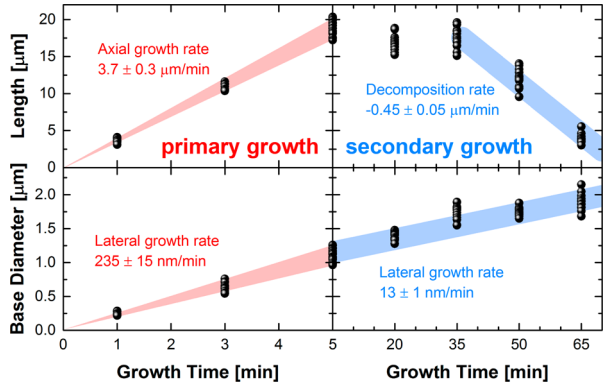


**Figure 2.** Statistics of the nanopillar evolution during the two-step growth process deduced from SEM analysis. The length and base diameter are given for increasing growth times.

growth mode with a constant aspect ratio of 16 between nanoneedle length and base diameter, similar to the observations in random InP nanopillar growth on silicon.[2]

The secondary growth aims to transfer the needle shape of the core into a pillar shape to improve the quality factor of the intrinsic optical cavity. Here, a higher temperature and V/III ratio are applied to consume the residual indium droplet at the tip, to preferentially decompose and redistribute defective crystal parts and to favor a lateral extension of the nanopillars.[13] The SEM images in Figure 2 show nanopillars after 20, 35, 50, and 65 min growth time. The formation of regular crystal facets becomes apparent under the growth conditions of secondary growth where the sidewalls of the nanopillars show 6-fold



DOI: 10.1021/acs.nanolett.7b00607
Nano Lett. 2017, 17, 2697−2702

symmetry. The evolution of the nanopillar base diameter (Figure 2 right) reveals a lateral growth rate of 13 ± 1 nm/min, being considerably slower than the radial growth rate in the primary growth. The needle tip is transferred to a flat top facet by moderate axial decomposition. For exceedingly thick shells, however, the axial decomposition rate dramatically accelerates and reaches up to −0.45 ± 0.05 μm/min (Figure 2 right). In the given low temperature regime, this controlled decomposition was found to yield the best results in terms of faceting and low tapering angles to achieve a high quality factor for the nanopillar cavity.

While all of the above was based on free-standing nanopillars in arrays with a pitch of 10 μm, a smaller spacing can be of relevance for certain applications as well. Therefore, Figure 3

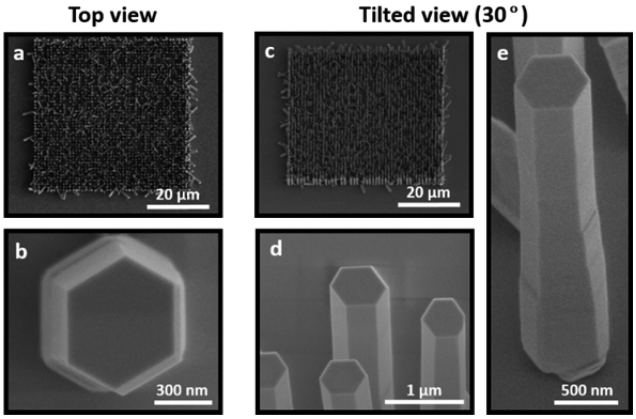


**Figure 3.** SEM images of an exemplary dense n-InP SAG nanopillar array on $SiO_2$/silicon nanomask featuring a small pitch of 1.2 μm: (a,b) Top view demonstrating a high yield and smooth top facets and (c,d,e) tilted view revealing regular side facets and a negligible tapering angle.

shows the result for an exemplary dense array with a small pitch of 1.2 μm. A high yield, i.e., the growth of exactly one vertical nanopillar per defined mask hole, can be achieved with the presented two-step growth process (Figure 3a,c). The hole depth of approximately 200 nm is crucial here for an effective suppression of parasitic nucleation of slanted satellite nanopillars. In dense arrays, the nanopillars feature flat top and smooth side facets as well (Figure 3b,d); however there is a clear difference regarding the nanopillar dimensions. The statistics (Figure S2) reveal a drop of nanopillar diameter and length to 30% with regard to free-standing nanopillars in a large pitch array. At the same time, nanopillars in dense arrays feature almost no difference in top and base diameter (Figure 3e) which indicates a higher effective V/III ratio.[13] We attribute this to a proximity effect during growth where nanopillars compete for constituents within their diffusion length, as illustrated in Figure S2a. The effect becomes visible for pitches smaller than 6 μm, which allows to estimate the diffusion length of indium under the applied growth conditions to be in the order of 3 μm.[24] Nonetheless, dense nanopillar arrays with high yield could be realized down to 0.5 μm pitch by an additional 3s TMI exposure prior to growth to provide enough indium to initiate nucleation.

The optical quality of the presented n-InP SAG nanopillars was investigated by microphotoluminescence spectroscopy (μPL) where individual nanopillars were excited by a tunable, mode-locked Ti:sapphire femtosecond laser guided through a 100x objective (NA = 0.70). The collected signal was analyzed in a spectrometer with 600 $mm^{-1}$ grating and detected by a charge-coupled device (CCD). Room temperature μPL spectra of an exemplary n-InP SAG nanopillar after 35 min of growth are presented in Figure S3a for increasing excitation power. The emission is centered at 862 nm with a fwhm as small as 40 nm. Figure S3b shows a log−log plot of the maximum PL intensity as a function of excitation power density with a slope close to 1. In addition, no wavelength shift is observed in Figure S3c with increasing excitation powers. These are strong indications of a radiative-dominant emission from a high-quality wurtzite crystal structure.[17,25] In the literature, 874 nm are reported for randomly nucleated, intrinsic InP nanopillars on silicon grown in the same temperature regime[3] and 877 nm of high-temperature, intrinsic InP SAG nanopillars on InP substrate.[21] The observed blueshift of 12 nm (19.7 meV) can be attributed to the doping-induced Burstein−Moss shift

$$\Delta E_g = \frac{\hbar^2}{2m_c^*}(3\pi^2 n_e)^{2/3}$$

with $n_e$ the electron concentration and $m_c^*$ the effective mass of the wurtzite $\Gamma_7$ conduction band.[26,27] Hence, an electron concentration of $4 \times 10^{17}$ $cm^{-3}$ can be estimated for the n-InP SAG nanopillars which is a reasonable basis for optoelectronic devices.

Given the high crystal quality of the gain medium, the lasing capability of n-InP SAG nanopillars is discussed in the following. Good modal confinement and low losses can be expected as the SAG nanopillars feature large diameters, regular side facets, and a low tapering angle. The flat top provides a good top reflector due to the large refractive index contrast of InP and air. The bottom reflection is significantly enhanced by the 140 nm thick $SiO_2$ mask as InP and silicon only have a minimal refractive index contrast. With a hole diameter of 0.35 μm and the pillar base diameter of 1.7 μm, the InP/silicon and InP/$SiO_2$ interfaces contribute 4% and 96% to the bottom mirror area, respectively. A rough estimation using the Fresnel formula yields top and bottom reflectivities of $R_\uparrow$ = 0.30 and $R_\downarrow$ = 0.16, respectively. Thus, a decent quality factor of the intrinsic optical nanopillar cavity can be expected.

Figure 4a shows the μPL spectra of an exemplary, optically pumped InP nanolaser at room temperature for increasing excitation power (140 fs pulse duration, 80 MHz repetition rate, spot diameter 1.5 μm). Two stimulated emission modes evolve from the broad spontaneous emission spectra, featuring a spacing of 11.5 nm and high suppression ratios of 16 and 6 dB, respectively. With a fwhm at threshold of $\Delta\lambda_{th}$ = 0.74 nm the Q-factor of the intrinsic nanopillar cavity can be estimated to be $Q \approx \lambda/\Delta\lambda_{th}$ = 1180.[28] The double-logarithmic light input versus light output plot (L−L curve) of the dominant mode in Figure 4b shows an S-shape behavior characteristic for lasing with a low threshold of 300 kW/$cm^2$. From the step size, the coupling efficiency of spontaneous emission to the nanopillar cavity can be estimated to be $\beta \sim 0.05$. These are excellent values compared to previously reported nanolasers on silicon emitting in the same spectral range: $Q \sim 308$ and $\beta \sim 0.0005$ in randomly grown InP nanoneedles on silicon,[3] $Q \sim 206$ and $\beta \sim 0.01$ in randomly grown InGaAs nanoneedles on silicon,[1] and $Q \sim 516$ and $\beta \sim 0.21$ in site-controlled GaAs/AlGaAs nanowires on $SiO_2$/silicon at 4 K.[29] The center wavelength versus excitation power density of the two stimulated emission modes and the spontaneous emission background are


DOI: 10.1021/acs.nanolett.7b00607
Nano Lett. 2017, 17, 2697−2702

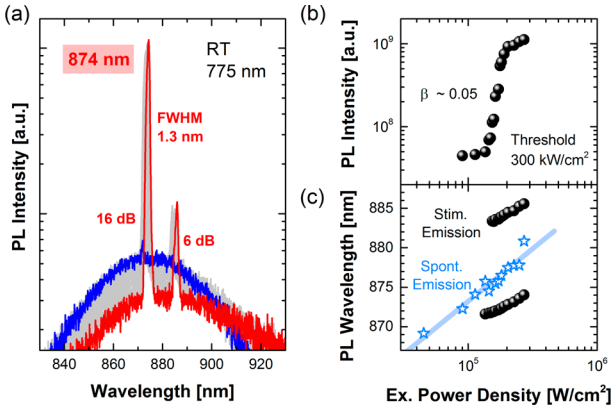


**Figure 4.** (a) Lasing spectra of an optically pumped n-InP SAG nanopillar (35 min growth time) for increasing excitation power (blue to red) with (b) corresponding L–L curve. (c) Wavelength shift of the two stimulated emissions and the spontaneous emission background versus excitation power density.

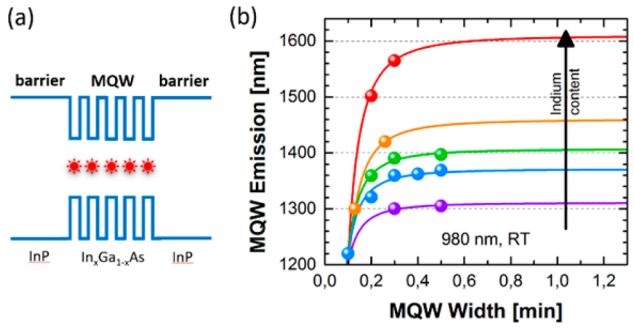


**Figure 5.** (a) Schematic of the electronic band structure of a 5*x* InGaAs MQW embedded in InP barriers. (b) Room temperature $\mu$PL emission of various site-controlled InP/InGaAs nanopillars versus MQW width in terms of growth time. The increase of the indium content can be observed in the saturation regime.

presented in Figure 4c. The redshift of the gain spectrum can be attributed to the temperature-induced bandgap shrinkage (14 nm per decade), while the resonance modes of the intrinsic cavity are less affected by temperature (8 nm per decade). To the best of our knowledge, this is the first room temperature III–V nanolaser monolithically integrated on silicon by a scalable, CMOS-compatible low-temperature process featuring position control in a vertical geometry. The emission wavelength of 875 nm is also perfectly situated in a commonly used spectral band of optic telecommunication.

The logical next step for optical communication would be to realize on-chip optical links via a coupling of the nanopillar emission to in-plane waveguides, as recently demonstrated in pioneering work for spontaneous emission.[30] However, a silicon-transparent nanolaser emission on a silicon platform has not been reported to the present day. For that purpose, InGaAs multiquantum-wells (MQW) can be incorporated, either in the primary growth (buried MQW) or in an additional third growth step (shell MQW). As the PL of shell MQWs was found to be significantly brighter, we will focus on this approach in the following. Site-controlled n-InP nanopillars after 20 min growth time served as a basis (Figure 1). In a third growth step five InGaAs multiquantum wells (MQW) were incorporated, each separated by 5 nm InP barriers and ultimately enclosed by 60 nm InP. A schematic of the resulting electronic band structure is given in Figure 5a. By adjusting the MQW width $d$ and the ternary $In_xGa_{1-x}As$ composition $x$, the emission wavelength can be tuned over a wide range in the infrared spectral region, covering the optimum telecommunication wavelengths 1.3 and 1.55 $\mu$m where losses and dispersion in glass fibers are minimal. To demonstrate that, various MQWs were grown at partial pressures of TBA = $3.9 \times 10^{-5}$ atm, TEGa = $1.3 \times 10^{-6}$ atm, and TMI = $1.2 \times 10^{-7}$ atm, respectively. When adjusting the MQW composition, both metal fluxes were changed proportionally to avoid a change of the MQW width. An overview of the emission wavelength versus MQW width in the fabricated SAG nanopillars is given in Figure 5b, recorded at room temperature under continuous-wave diode laser excitation (980 nm, 40 $\mu$W). For decreasing MQW width a blueshift is clearly observed, following the well-known $\Delta E \propto d^{-2}$ behavior of the quantum confinement effect. For increasing MQW width, the emission saturates as no quantum confined Stark effect (QCSE) is present along the nonpolar $\{10\bar{1}0\}$ nanopillar sidewalls. Thus, the $In_xGa_{1-x}As$ compositions can be estimated from these saturation wavelengths and are given in Figure 5b.[31] In order to minimize the impact of strain accumulation in the MQW stack, only thin MQWs are investigated here. Furthermore, the results refer to SAG nanopillars in 10 $\mu$m pitch arrays. The pitch dependence of the MQW emission due to the proximity effect is presented in the Supporting Information (Figure S4).

After discussing how to tune the MQW emission, this raises the question if the MQW can interact efficiently with the InP nanopillar cavity to achieve lasing? The SEM image of an exemplary 10 $\mu$m pitch InP/InGaAs nanopillar is presented in Figure 6a to confirm the preservation of the smooth faceting, the flat top, and the low tapering angle. The corresponding $\mu$PL spectra are presented in Figure 6b for increasing excitation power, featuring a room temperature emission centered at the telecommunication wavelength of 1.3 $\mu$m. The ternary alloy in the MQW leads to a broader fwhm of 140 nm compared to the binary InP emission in Figure S3. Sharp equidistant peaks evolve in the spectrum with a spacing of 8.18 nm and a fwhm of 3.5 nm which can be attributed to Fabry-Pérot modes whose spacing is given by

$$\Delta\lambda_{FP} = \frac{\lambda^2}{2L\left[n - \lambda\frac{dn}{d\lambda}\right]} = \frac{\lambda^2}{2Ln_g}$$

with $L$ the cavity length, $n$ the refractive index, and $n_g$ the group refractive index.[32,33] With $L$ = 23.5 $\mu$m deduced from SEM, this yields a group refractive index of $n_g$ = 4.4. The $\mu$PL spectra at low temperature are presented in Figure 6c for increasing excitation power density (blue to red). A single lasing mode evolves at 1.21 $\mu$m with a high suppression ratio of 16 dB while other Fabry-Pérot modes are not amplified. The fwhm at threshold of $\Delta\lambda_{th}$ = 1.12 nm indicates a $Q$-factor of the nanopillar cavity as high as $Q = \lambda/\Delta\lambda_{th}$ = 1078. The corresponding L–L curve (Figure 6d) reveals a threshold of 36 kW/cm$^2$ and a coupling of the spontaneous MQW emission to the nanopillar cavity in the order of $\beta \sim 0.03$, slightly lower compared to the InP lasing in Figure 4. The spectrum of the spontaneous emission shows a blueshift with increasing excitation power density (Figure 6e), which indicates band filling in the thin quantum wells. Above the threshold, the clamping of the spontaneous emission is observed where both gain spectrum and cavity follow a thermally induced redshift. This is the first demonstration of a nanolaser on silicon substrate emitting at a silicon-transparent wavelength, which


DOI: 10.1021/acs.nanolett.7b00607
Nano Lett. 2017, 17, 2697–2702

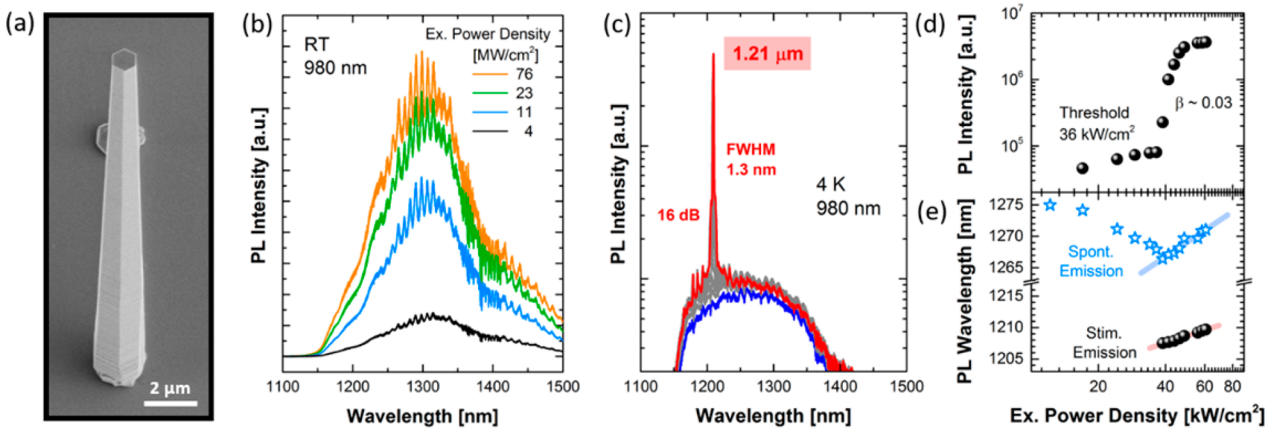


**Figure 6.** (a) SEM image of an exemplary InP SAG nanopillar with InGaAs MQW standing in a 10 $\mu$m pitch array. (b) Room-temperature $\mu$PL spectra of a 5 nm MQW for increasing excitation power. The emission is centered at 1.3 $\mu$m and features Fabry-Pérot modes with a spacing of 8.18 nm. (c) Lasing spectra at low temperature for increasing excitation power (blue to red) with (d) a corresponding L−L curve. (e) Wavelength shift of the stimulated emission and the spontaneous emission background versus excitation power density.

opens up a whole new playground for nanoscale on-chip optical links.

In summary, we demonstrated the site-controlled growth of InP nanopillars on silicon by utilizing $SiO_2$ masks and a two-step growth procedure. Both nanomask fabrication and MOCVD growth are scalable to large wafer sizes, do not require foreign catalysts, and stay within the thermal budget of silicon-based CMOS post-processing, providing full compatibility with state-to-the-art silicon electronics. The regular wurtzite faceting of the nanopillars with low tapering and the enhanced reflectivity in the bottom due to the $SiO_2$ nanomask form an intrinsic optical cavity with high quality factor which promotes their lasing capability. Furthermore, we demonstrated that the nanopillar emission can be tuned over a wide range by an incorporation of InGaAs MQWs. As a result, we could demonstrate lasing at 0.87 and 1.21 $\mu$m within two important optical telecommunication bands. To the best of our knowledge, this is the first demonstration of site-controlled III−V nanolasers monolithically integrated on silicon with a silicon-transparent emission wavelength. The presented process is believed to bring electrically driven nanolasers on a silicon platform close within reach, which would be a breakthrough on the route to energy-efficient on-chip optical links.

## ■ ASSOCIATED CONTENT

### Supporting Information

The Supporting Information is available free of charge on the ACS Publications website at DOI: 10.1021/acs.nanolett.7b00607.

An illustration of the growth procedure, a power-dependent photoluminescence measurement of site-selective InP nanopillars, and a study of the proximity effect on the InP nanopillar geometry and the InGaAs MQW emission wavelength (PDF)

## ■ AUTHOR INFORMATION


### Corresponding Author

*E-mail: cch@berkeley.edu.

### ORCID

Fabian Schuster: 0000-0001-6637-4564

Gilliard N. Malheiros-Silveira: 0000-0002-5176-3812

Saniya Deshpande: 0000-0002-7760-6604

Connie J. Chang-Hasnain: 0000-0002-5341-6267


### Notes

The authors declare no competing financial interest.

## ■ ACKNOWLEDGMENTS

The authors thank E. Kolev for his guidance in MOCVD maintenance, K. T. Cook for the help in nanomask fabrication, and I. Bhattacharya for valuable support with the PL setup. We acknowledge research support of NSF Award 1335609, ECCS-0939514, and the Singapore National Research Foundation Singapore−Berkeley Research Initiative for Sustainable Energy (SinBeRISE) Program NRF-CRP14-2014-03.

## ■ REFERENCES


(1) Chen, R.; Tran, T.-T. D.; Ng, K. W.; Ko, W. S.; Chuang, L. C.; Sedgwick, F. G.; Chang-Hasnain, C. J. *Nat. Photonics* **2011**, *5*, 170.

(2) Ren, F.; Ng, K. W.; Li, K.; Sun, H.; Chang-Hasnain, C. J. *Appl. Phys. Lett.* **2013**, *102*, 012115.

(3) Li, K.; Sun, H.; Ren, F.; Ng, K. W.; Tran, T.-T. D.; Chen, R.; Chang-Hasnain, C. J. *Nano Lett.* **2014**, *14*, 183.

(4) Ko, W. S.; Tran, T.-T. D.; Bhattacharya, I.; Ng, K. W.; Sun, H.; Chang-Hasnain, C. J. *Nano Lett.* **2015**, *15*, 4961.

(5) Takeuchi, H.; Wung, A.; Sun, X.; Howe, R. T.; King, T.-J. *IEEE Trans. Electron Devices* **2005**, *52*, 2081.

(6) Lu, F.; Tran, T.-T. D.; Ko, W. S.; Ng, K. W.; Chen, R.; Chang-Hasnain, C. J. *Opt. Express* **2012**, *20*, 12171.

(7) Mårtensson, T.; Borgström, M.; Seifert, W.; Ohlsson, B.; Samuelson, L. *Nanotechnology* **2003**, *14*, 1255.

(8) Mårtensson, T.; Carlberg, P.; Borgström, M.; Montelius, L.; Seifert, W.; Samuelson, L. *Nano Lett.* **2004**, *4*, 699.

(9) Dalacu, D.; Kam, A.; Austing, D. G.; Wu, X.; Lapointe, J.; Aers, G. C.; Poole, P. J. *Nanotechnology* **2009**, *20*, 395602.

(10) Wang, J.; Plissard, S.; Hocevar, M.; Vu, T. T.; Zehender, T.; Immink, G. G.; Verheijen, M. A.; Haverkort, J.; Bakkers, E. P. *Appl. Phys. Lett.* **2012**, *100*, 053107.

(11) Kawaguchi, K.; Sudo, H.; Matsuda, M.; Ekawa, M.; Yamamoto, T.; Arakawa, Y. *Appl. Phys. Lett.* **2014**, *104*, 063102.

(12) Inari, M.; Takeda, J.; Motohisa, J.; Fukui, T. *Phys. E* **2004**, *21*, 620.

(13) Mohan, P.; Motohisa, J.; Fukui, T. *Nanotechnology* **2005**, *16*, 2903.

(14) Ding, Y.; Motohisa, J.; Hua, B.; Hara, S.; Fukui, T. *Nano Lett.* **2007**, *7*, 3598.

(15) Chu, H.-J.; Yeh, T.-W.; Stewart, L.; Dapkus, P. D. *Phys. Stat. Sol. C* **2010**, *7*, 2494.




DOI: 10.1021/acs.nanolett.7b00607
*Nano Lett.* 2017, 17, 2697−2702

(16) Kitauchi, Y.; Kobayashi, Y.; Tomioka, K.; Hara, S.; Hiruma, K.; Fukui, T.; Motohisa, J. *Nano Lett.* **2010**, *10*, 1699.
(17) Ikejiri, K.; Kitauchi, Y.; Tomioka, K.; Motohisa, J.; Fukui, T. *Nano Lett.* **2011**, *11*, 4314.
(18) Goto, H.; Nosaki, K.; Tomioka, K.; Hara, S.; Hiruma, K.; Motohisa, J.; Fukui, T. *Appl. Phys. Express* **2009**, *2*, 035004.
(19) Wallentin, J.; Anttu, N.; Asoli, D.; Huffman, M.; Åberg, I.; Magnusson, M. H.; Siefer, G.; Fuss-Kailuweit, P.; Dimroth, F.; Witzigmann, B.; Xu, H. Q.; Samuelson, L.; Deppert, K.; Borgström, M. T. *Science* **2013**, *339*, 1057.
(20) Yoshimura, M.; Nakai, E.; Tomioka, K.; Fukui, T. *Appl. Phys. Express* **2013**, *6*, 052301.
(21) Gao, Q.; Saxena, D.; Wang, F.; Fu, L.; Mokkapati, S.; Guo, Y.; Li, L.; Wong-Leung, J.; Caroff, P.; Tan, H. H.; Jagadish, C. *Nano Lett.* **2014**, *14*, 5206.
(22) Watanabe, Y.; Hibino, H.; Bhunia, S.; Tateno, K.; Sekiguchi, T. *Phys. E* **2004**, *24*, 133.
(23) Wang, Z.; Tian, B.; Paladugu, M.; Pantouvaki, M.; Le Thomas, N.; Merckling, C.; Guo, W.; Dekoster, J.; Van Campenhout, J.; Absil, P.; Van Thourhout, D. *Nano Lett.* **2013**, *13*, 5063.
(24) Schuster, F.; Hetzl, M.; Weiszer, S.; Garrido, J. A.; De La Mata, M.; Magen, C.; Arbiol, J.; Stutzmann, M. *Nano Lett.* **2015**, *15*, 1773.
(25) Tran, T.-T. D.; Sun, H.; Ng, K. W.; Ren, F.; Li, K.; Lu, F.; Yablonovitch, E.; Chang-Hasnain, C. J. *Nano Lett.* **2014**, *14*, 3235.
(26) Hamberg, I.; Granqvist, C.; Berggren, K.-F.; Sernelius, B. E.; Engström, L. *Phys. Rev. B: Condens. Matter Mater. Phys.* **1984**, *30*, 3240.
(27) De, A.; Pryor, C. E. *Phys. Rev. B: Condens. Matter Mater. Phys.* **2010**, *81*, 155210.
(28) Hua, B.; Motohisa, J.; Ding, Y.; Hara, S.; Fukui, T. *Appl. Phys. Lett.* **2007**, *91*, 131112.
(29) Mayer, B.; Janker, L.; Loitsch, B.; Treu, J.; Kostenbader, T.; Lichtmannecker, S.; Reichert, T.; Morkötter, S.; Kaniber, M.; Abstreiter, G.; Gies, C.; Koblmüller, G.; Finley, J. J. *Nano Lett.* **2016**, *16*, 152.
(30) Kim, H.; Farrell, A. C.; Senanayake, P.; Lee, W.-J.; Huffaker, D. L. *Nano Lett.* **2016**, *16*, 1833.
(31) Nahory, R. E.; Pollack, M. A.; Johnston, W. D., Jr; Barns, R. L. *Appl. Phys. Lett.* **1978**, *33*, 659.
(32) Duan, X.; Huang, Y.; Agarwal, R.; Lieber, C. M. *Nature* **2003**, *421*, 241.
(33) Malheiros-Silveira, G. N.; Bhattacharya, I.; Deshpande, S.; Skuridina, D.; Lu, F.; Chang-Hasnain, C. J. *Opt. Express* **2017**, *25*, 271.



DOI: 10.1021/acs.nanolett.7b00607
*Nano Lett.* 2017, 17, 2697−2702